Magnetic Analysis of Skew Effect in Surface-Mounted Permanent Magnet Machines With Skewed Slots

Haijun Zhuang[1], Shuguang Zuo[1], Zhixun Ma[2], Qiang Yu[3], Zhipeng Wu[1], and Chang Liu[1]

[1]School of Automotive Studies, Tongji University, Shanghai 201804, China
[2]National Maglev Transportation Engineering Research and Development Center, Tongji University, Shanghai 201804, China
[3]School of Information and Control Engineering, China University of Mining and Technology, Xuzhou 221116, China

Surface-mounted permanent magnet (SPM) machines with skewed slots as vehicle drives are widely used. Due to skewed slots, electromagnetic characteristics are modulated by the skew effect. To analyze the skew effect, Maxwell's equations-based 3-D analytical model is proposed. Based on differences in 3-D air-gap flux density distribution, the mechanism by which the skew effect modulates cogging torque, flux linkage, and back electromotive force (EMF) is investigated. The effectiveness of the theory about the skew effect is verified by both the finite element method (FEM) and the experimental result.

Index Terms— **Analytical model, cogging torque, skew effect, surface-mounted permanent magnet (SPM) machine.**

I. Introduction

DUE to high power density and efficiency, surface-mounted permanent magnet (SPM) motors are widely used in electric vehicles [1], [2]. However, to pursue higher performance, the magnetic energy of PMs becomes larger, resulting in more intense cogging torque. Further, undesirable vibration and noise can be generated [3], [4]. Therefore, various means have been used to suppress cogging torque, with the machine-based perspective, such as auxiliary slots, specific the slot width or the pole arc coefficient of PMs, as well as skewing, etc. [5], [6], [7]. Among many methods, due to unchanging motor parameters, the skewing becomes a convenient means to suppress the cogging torque and optimize the waveform of the back electromotive force (EMF); in addition, considering the stator structure is relatively malleable in the SPM machine, skewed slots are of course the preferred choice. Hence, the skewing represents the skewed slot in this article. However, due to the skewing, the air-gap flux density is modulated by the skew effect in the axial direction, which greatly increases the difficulty of electromagnetic analysis.

The high accuracy is the core feature of FEM, which makes it widely used in electromagnetic analysis [8], [9]. However, the sensitivity of air-gap magnetic field changes requires precise calculations, which causes a time-consuming solution process [10]. Compared with time-consuming FEM, the analytical method, mainly including the equivalent magnetic circuit method and Maxwell's equations-based analytical model, is faster and more competent to investigate the mechanism of electromagnetic characteristics. Although nonlinear factors can be considered by the equivalent magnetic circuit method, the nonnegligible tangential flux density is unavailable [11], [12]. Therefore, in order to calculate the radial and tangential flux density, the Maxwell's equations-based analytical model is utilized. The air-gap flux density is obtained by the solved magnetic vector potential. When the air-gap magnetic resistance does not change drastically, each component is regarded as a coaxial hollow cylinder, and thus the multilayer model is used [13], [14], [15]. When the air-gap magnetic resistance changes drastically, the slots and teeth are divided into domains and connected to the yoke, and the subdomain model is used [16], [17].

For the SPM machine, the previous studies are based on 2-D electromagnetic analytical models. However, as to the machine considering skewing, the 2-D electromagnetic analytical model is not effective due to the skew effect. Therefore, the energy method and Fourier series analysis are utilized to derive the cogging toque considering skewing. The air-gap flux is calculated by solving Maxwell's equations in polar coordinates, which makes the cogging torque obtained by manipulating the 2-D analytical model [18]. Meanwhile, the multisegment method is widely used to investigate the motor considering skewing [19]. In this method, the motor consists of a limited number of segmented motors in the axial direction. Therefore, the quasi-3-D electromagnetic characteristics are calculated by superimposing that of each segment. The features of each segmented motor are as follows: (1) the same amplitude and (2) phase difference. However, the author does not investigate the mechanism by which the cogging torque and back EMF are modulated by the skew effect. Meanwhile, the multisegment method cannot consider: (1) the axial distribution of MMF of PMs and winding current, that is, axial harmonics and (2) the end effect. Therefore, for the machine considering skewing, the electromagnetic analytical model is inevitable to expand.

As to cogging torque, it is not only related to the air-gap flux density but also to the slotting effect. For the slotting effect, subdomain models and conformal mapping methods can be effectively considered. In the subdomain model, when calculating the air-gap flux density, the slotting effect has been considered. For conformal mapping, the slotting effect can be

Manuscript received 6 August 2022; revised 11 September 2022; accepted 12 September 2022. Date of publication 22 September 2022; date of current version 28 November 2022. Corresponding author: S. Zuo (e-mail: sgzuo@tongji.edu.cn).

Color versions of one or more figures in this article are available at https://doi.org/10.1109/TMAG.2022.3208696.

Digital Object Identifier 10.1109/TMAG.2022.3208696

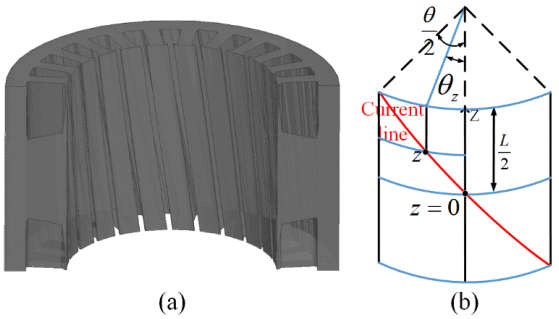

Fig. 1. SPM machine with skewed slots. (a) Schematic model. (b) Analytical model.

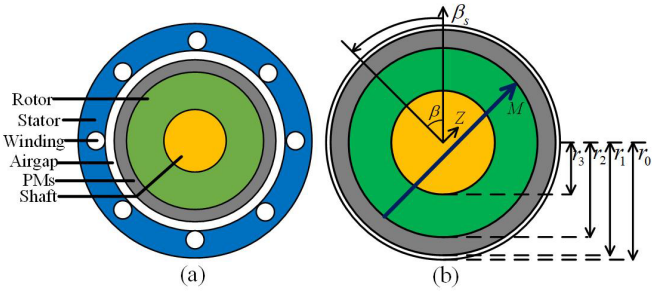

Fig. 2. 3-D analytical model. (a) Overview. (b) Rotor with cylindrical coordinates defined.

taken into account by the complex relative permeance function, which works on the nonslotted motor as an additional function. In [20], the principle of conformal mapping is proposed, but the uniform expression of the complex relative permeance function is not given. Therefore, in [21], a novel method is proposed to conduct the uniform expression of the complex relative permeance function, which solves Laplace's equation over a portion of the slotted air gap by imposing appropriate boundary conditions in the slot opening region. For the motor with skewed slots, the slotting effect is also affected by the skew effect, so it is necessary to further revise the slotting effect model.

Hence, for the SPM machine considering skewing, Maxwell's equations-based 3-D electromagnetic analytical model is proposed to investigate the mechanism by which the cogging torque and back EMF are modulated by the skew effect. The organization is as follows. In Section II, Maxwell's equations-based 3-D analytical model is established, which focuses on the modeling of the skewing. In Section III, based on the differences in electromagnetic characteristics with and without considering skewing, the modulation principle of the skew effect is investigated. In Section IV, the effectiveness of magnetic analysis of the skew effect is verified by 3-D FEM. In Section V, in order to further verify the theory about the skew effect, SPM machines with straight and skewed slots are manufactured and tested.

II. Analytical Model

The schematic and analytical model of the SPM machine with skewed slots are shown in Fig. 1(a) and (b). Due to skewed slots, the MMF of winding current that interacts with PM and the slotting effect present dislocation distributions at different axial positions. By taking the center of axial length as the starting point, the MMF of the terminal winding current that interacts with PM and the terminal slotting effect are shifted $\theta/2$ in phase relative to the starting point, where θ is the overall angle of the skewed slot. Correspondingly, for any axial length, the MMF of winding current, and the slotting effect are shifted in phase, which is expressed by the angle

$$\theta_z = \pm\theta \cdot \frac{z}{L}. \tag{1}$$

Here, θ_z is the shifted angle of MMF of current and the slotting effect under any axial length. z and L are either the axial length or the axial length of PM, respectively.

In order to analyze the modulation principle of the skew effect on electromagnetic characteristics, the Maxwell's equations-based 3-D analytical model is proposed, which is shown in Fig. 2. The multilayer structure is the prominent characteristic of the analytical model. It consists of a stator, air gap, PMs, rotor core, and shaft. Meanwhile, the stator can be ignored. The reasons are as follows: (1) infinite magnetic permeability and (2) layer distributed winding current. Therefore, the core of the analytical model is rotor components, which is shown in Fig. 2(b). It should be noted that the neglected slotting effect is considered by the complex relative permeance function, which acts on the 3-D analytical model as an additional function.

In Fig. 2(b), the cylindrical coordinate $r - \beta - z$ is defined as well. The β_s represents the stator fixed coordinate system, which is a global reference system. This is because the motor is a synchronous machine. Here, it should be noted that β is the electrical angle, which can convert to machine angle by $\beta = p \cdot \alpha$. where α is the machine angle. Next, the direction of rotation is counterclockwise. Then, each layer is numbered to calculate conveniently, which is starting from $i = 1$, until the shaft layer. Meanwhile, the subscript r represents the radius of each layer, respectively.

The following assumptions should be made in the 3-D electromagnetic analytical model.

1) PMs do not demagnetize.
2) The stator and rotor cannot be saturated.

Therefore, the joint air-gap flux density is a linear superposition of that excited by PMs and current, respectively. Based on the difference in electromagnetic characteristics, the modulation principle of the skew effect is obtained. Fig. 3 shows the analysis flow, with a couple of steps. The first step is to establish the 3-D analytical model, in particular, to model the skewing. The calculation method is organized as follows. Starting from MMF distribution of winding current with emphasis on skewing modeling and end effect in Section II-A, the MMF distribution of PMs in Section II-B, deduction of the magnetic field is performed in Section II-C, revise of slotting effect considering skewing in Section II-D. In the second step, the electromagnetic characteristics of different skew angles are obtained and compared, and then the skew effect is investigated.

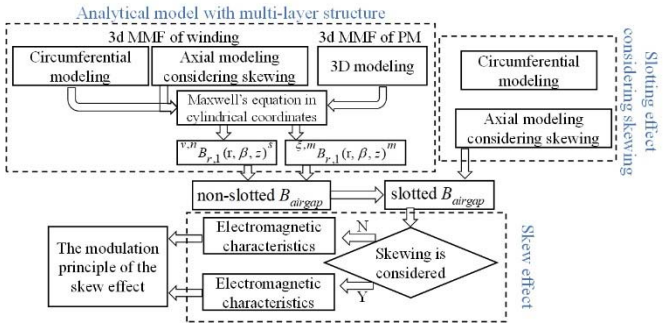

Fig. 3. Flowchart of the analytical model.

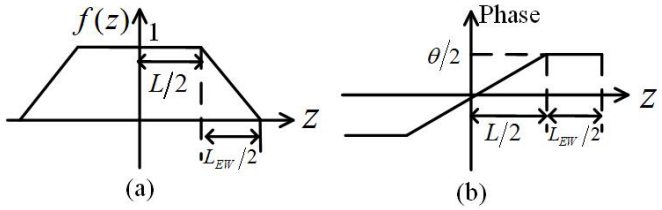

Fig. 4. Axial distribution. (a) Axial function of MMF. (b) Phase function of MMF.

A. MMF of the Winding Current

According to Ampere's law, the MMF of winding current can be written as

$$\Theta(\beta) = N(\beta)i \tag{2}$$

where $\Theta(\beta)$ is MMF of the winding current, $N(\beta)$ is the winding function, and i is the stator current.

For the winding function, modeling from a single coil and the all of one phase and finally all phases using Fourier method. Meanwhile, for the ac machine, it is assumed that the current is sinusoidal. Therefore, the circumferential MMF of the winding current can be derived as

$$\begin{aligned} {}^{\upsilon}\Theta(\beta,t) &= \frac{\sqrt{2}\cdot W\cdot I\cdot N_{\text{ph}}}{\upsilon\pi}\cdot {}^{\upsilon}\xi_z\cdot {}^{\upsilon}\xi_s\cdot {}^{\upsilon}\xi_N\cdot e^{j[\omega t-\upsilon_p\beta]} \\ \upsilon_p &= \frac{\upsilon}{p} = 2\cdot a\cdot N_{\text{ph}}+1, \quad a=0,\pm1,\pm2,\ldots \end{aligned} \tag{3}$$

where superscripts υ indicates circumference harmonics. W is the total number of turns in one winding, and the value is $W = 2\cdot p\cdot q\cdot N_c$. I is the effective value of the current, and ω is the frequency of the current. N_{ph} is the number of phases. ${}^{\upsilon}\xi_s$, ${}^{\upsilon}\xi_N$, and ${}^{\upsilon}\xi_z$ are, respectively, the short pitch factor, slot opening factor, and the distributed factor.

Considering the skew effect and end effect, the axial distribution and phase function of MMF are shown in Fig. 4(a) and (b), respectively. For windings interacting with PMs, the phase of MMF linearly changes with axial position, but the amplitude keeps constant. For the end winding, due to nonexistent steel, the amplitude of MMF attenuates to zero in a trapezoidal form, but the phase remains unchanged. Therefore, the axial distribution function ${}^{n}f(z)$ can be expressed by the Fourier series as

$${}^{n}f(z) = {}^{n}b\cos\left(\frac{\pi}{L_Z}nz\right) \tag{4}$$

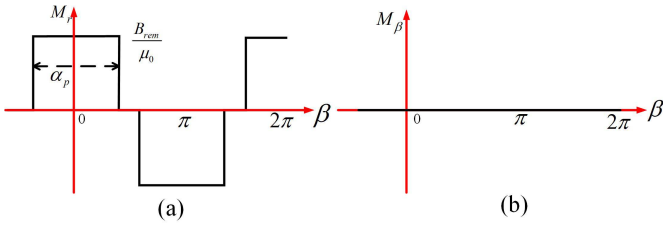

Fig. 5. Residual magnetization vector model. (a) Distribution of radial magnetization. (b) Distribution of tangential magnetization.

with

$$\begin{aligned} {}^{n}b &= \frac{1}{\pi n}\left(4+\frac{L-2L_1}{L_{\text{EW}}}\right)\sin\left(\frac{\pi\cdot L_1\cdot n}{L}\right) \\ &\quad -\frac{2L_z}{L_{\text{EW}}\pi^2n^2}\left(\cos\left(\frac{\pi\cdot L_1\cdot n}{L_z}\right)-\cos\left(\frac{\pi\cdot L\cdot n}{L_z 2}\right)\right) \end{aligned} \tag{5}$$

$$L_1 = \frac{L}{2}+2L_{\text{EW}}, \quad L_z = L+2L_{\text{EW}} \tag{6}$$

where n is axial harmonics, and L_{EW} is the length of end winding.

To sum up, the 3-D MMF of winding current considering skewing can be written as

$$\begin{aligned} {}^{\upsilon,n}\Theta(\beta,z,t) &= \frac{\sqrt{2}\cdot W\cdot I\cdot N_{\text{ph}}}{\upsilon\pi}\cdot {}^{n}b\cdot\cos\left(\frac{\pi}{L_z}nz\right) \\ &\quad \cdot {}^{\upsilon}\xi_z\cdot {}^{\upsilon}\xi_s\cdot {}^{\upsilon}\xi_N\cdot e^{j\left[\omega t-\upsilon_p\left(\beta-p\cdot\frac{z}{L}\cdot\theta\right)\right]}. \end{aligned} \tag{7}$$

B. MMF of PMs

For radial magnetization, the radial and tangential distribution of magnetization of PMs are shown in Fig. 5, where M_r and M_β are, respectively, the radial and tangential components of magnetization. Due to radial magnetization, the amplitude of M_β is zero. Meanwhile, the M_r is expressed by the Fourier series as

$$M_r(\beta) = \sum_{\xi}{}^{\xi}M_r\cdot e^{-j\xi\beta} \tag{8}$$

with

$${}^{\xi}M_r = 2\frac{B_{\text{rem}}}{\mu_0}\alpha_p\frac{\sin\left(\frac{\xi\pi\alpha_p}{2}\right)}{\frac{\xi\pi\alpha_p}{2}} \tag{9}$$

where ξ is the circumferential harmonic of PMs, B_{rem} is the remanence flux density, and μ_0 is the permeability of vacuum.

The axial distribution of magnetization is shown in Fig. 6, which can be written by the Fourier series as

$${}^{m}f(z) = 2\sum_{m}\frac{\sin\left(\frac{m\pi}{2}\right)}{\frac{m\pi}{2}}\cos\left(\frac{m\pi}{L}z\right) = \sum_{m}{}^{m}a\cos\left(\frac{m\pi}{L}z\right) \tag{10}$$

with

$${}^{m}a = 2\cdot\frac{\sin\left(\frac{m\pi}{2}\right)}{\frac{m\pi}{2}} \tag{11}$$

where m is the axial harmonic.

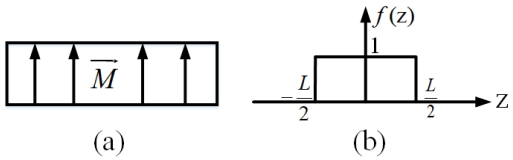

Fig. 6. Axial distribution of magnetization. (a) Axial distribution of magnetization model. (b) Axial distribution function.

Therefore, due to the nonaffected by skew effect, the 3-D magnetization can be expressed as

$$^{\xi,m}M(\beta,z) = {}^{\xi}M_r \cdot {}^{m}a \cdot \cos\left(\frac{m\pi}{L}z\right) \cdot e^{-j\xi\beta}. \tag{12}$$

C. Maxwell's Equations

In Maxwell's equations-based analytical model, the magnetic vector potential A is the core parameter during the calculated process. This is because A relates to the flux density B by $B\text{rot}(A)$. Due to the concentrated distributed current, the current does not flow radially. Meanwhile, due to the radial magnetizing direction of PM, the equivalent current only flows in the circumferential and axial directions. Therefore, the radial component of A can be ignored.

For any layer i, due to the existence of PMs, Maxwell's equations have different expressions in the cylindrical coordinates. For the layer of PMs, Maxwell's equations can be expressed as

$$\begin{cases} \frac{1}{r}\frac{\partial}{\partial r}{}^{\xi,\kappa}A_{\beta,i} + \frac{\partial^2}{\partial r^2}{}^{\xi,\kappa}A_{\beta,i} + \frac{1}{r^2}\frac{\partial^2}{\partial \beta^2}{}^{\xi,\kappa}A_{\beta,i} + \frac{\partial^2}{\partial z^2}{}^{\xi,\kappa}A_{\beta,i} \\ \qquad = \mu_i\gamma_i\frac{\partial}{\partial t}{}^{\xi,\kappa}A_{\beta,i} - \mu_0\frac{\partial}{\partial z}{}^{\xi,\kappa}M_{r,z} \\ \frac{1}{r}\frac{\partial}{\partial r}{}^{\xi,\kappa}A_{z,i} + \frac{\partial^2}{\partial r^2}{}^{\xi,\kappa}A_{z,i} + \frac{1}{r^2}\frac{\partial^2}{\partial \beta^2}{}^{\xi,\kappa}A_{z,i} + \frac{\partial^2}{\partial z^2}{}^{\xi,\kappa}A_{z,i} \\ \qquad = \mu_i\gamma_i\frac{\partial}{\partial t}{}^{\xi,\kappa}A_{z,i} + \mu_0\frac{1}{r}\frac{\partial}{\partial \beta}{}^{\xi,\kappa}M_{r,z} \end{cases} \tag{13}$$

where μ_i and γ_i are the relative permeability and the conductivity of layer i, respectively. For layers without PMs, due to no magnetization, the amplitude of M is equal to zero, which leads to $\mu_0(\partial/\partial z)^{\xi,\kappa}M_{r,z} = 0$ and $\mu_0(1/r)(\partial/\partial\beta)^{\xi,\kappa}M_{r,z} = 0$.

The diffusion equation is solved by the separation variable method, and A is obtained by solving Bessel's equation through boundary conditions. The expressions of A of the air gap layer under PM and current excitation are shown in Appendixes I and II, respectively.

D. Slotting Effect

The slotting effect is considered by the conformal mapping method, which works as an additional function for the 3-D analytical model. The slotting effect calculated by the complex relative permeance function can be written as

$$\lambda^*(\beta,z) = \lambda_a + j\lambda_b \tag{14}$$

where λ_a and λ_b represent the real and imaginary parts.

Due to skewing, the slotting effect is modulated by the skew effect in phase, which has the same distribution as the phase of the current MMF. Therefore, the real and imaginary parts are corrected to

$$\lambda_a = \lambda_{a0} + \sum_{\mu=1}^{\infty}\lambda_{a\mu}\cos\left[\mu\cdot Q_s\left(\alpha + \frac{z}{L}\cdot\theta\right)\right] \tag{15}$$

$$\lambda_b = \sum_{\mu=1}^{\infty}\lambda_{b\mu}\sin\left[\mu\cdot Q_s\left(\alpha + \frac{z}{L}\cdot\theta\right)\right] \tag{16}$$

where Q_s is the number of slots, μ is the circumferential harmonic of the slotting effect. λ_{a0} is the constant of the real part, $\lambda_{a\mu}$ and $\lambda_{b\mu}$ are the coefficients of the real and imaginary parts, respectively.

III. Electromagnetic Characteristics

A. Air-Gap Flux Density

By disabling armature current, only PMs are working as the magnetic source, and the radial air-gap flux density can be expressed as

$$^{\xi,m}B_{r,1}(r,\beta,z)^m = B_{r,1}(r,\beta,z)^m \cdot \cos\left(m\frac{\pi}{L}z\right) \cdot e^{j(\xi\cdot w\cdot t - \xi\cdot\beta)}\cdot\lambda_a \tag{17}$$

where $B_{r,1}(r,\beta,z)^m$ is the amplitude of the flux density excited by PMs, which can be expressed as

$$B_{r,1}(r,\beta,z)^m = -j\frac{r_0}{\xi}\left[\left(\frac{\xi}{r_0}\right)^2 + \left(\frac{m\pi}{L}\right)^2\right]\cdot{}^{m}a \cdot{}^{\xi,m}C_5^m\cdot\left[I_\xi\left({}^{m}k_1\cdot r_0\right) + {}^{\xi,m}C_6^m\cdot K_\xi\left({}^{m}k_1\cdot r_0\right)\right] \tag{18}$$

where $^{\xi,m}C_5^m$ and $^{\xi,m}C_6^m$ are the constant coefficients, which are shown in Appendix I. I_ξ and K_ξ are the modified Bessel function of the first and second kind.

In analogy by disabling PMs excitation, only armature coils are working as magnetic sources, the radial air-gap flux density can be expressed as

$$^{\upsilon,n}B_{r,1}(r,\beta,z)^s = B_{r,1}(r,\beta,z)^s\cdot\cos\left(n\frac{\pi}{L_Z}z\right)\cdot e^{j\left[wt - \upsilon_p\left(\beta - p\frac{z}{L}\cdot\theta\right)\right]}\cdot\lambda_a \tag{19}$$

where $B_{r,1}(r,\beta,z)^S$ is the amplitude of the flux density excited by winding current, which can be expressed as

$$B_{r,1}(r,\beta,z)^s = -j\frac{r_0}{\upsilon_p}\left[\left(\frac{\upsilon_p}{r_0}\right)^2 + \left(\frac{n\pi}{L_z}\right)^2\right]\cdot{}^{n}b \cdot{}^{\upsilon,n}C_5^S\cdot\left[I_{\upsilon_p}\left({}^{n}k_1 r_0\right) + {}^{\upsilon,n}C_6^S K_{\upsilon_p}\left({}^{n}k_1 r_0\right)\right]. \tag{20}$$

Finally, the joint air-gap flux density is obtained by superposition of magnetic fields of PMs and coil, which can be written as

$$^{\xi,m,\upsilon,n}B_{r,1}(r,\beta,z) = {}^{\xi,m}B_{r,1}(r,\beta,z)^m + {}^{\upsilon,n}B_{r,1}(r,\beta,z)^s. \tag{21}$$

TABLE I

SOURCE, CIRCUMFERENTIAL CONDITION, FREQUENCY, AND AMPLITUDE OF COGGING TORQUE CONSIDERING SKEWING

Source	Circumferential/axial condition	Frequency	Amplitude
Interaction of PM field with real part constant and imaginary part coefficient of slotting effect	$\mu Q_s - 2\xi p = 0$ $m \neq \mu$	2ξ	$-\frac{r_0^2 \cdot \lambda_0 \cdot \lambda_{b\mu}}{2\mu_0} \cdot \left\|B_{r,1}(\mathrm{r},\beta,z)^m\right\|^2 \cdot L \cdot \pi \cdot \sin(\mu Q_s \frac{\theta}{2}) \left\{ \begin{array}{l} \frac{1}{\mu Q_s \frac{\theta}{2}} + \frac{1}{2m\pi - \mu Q_s \theta} \\ -\frac{1}{2m\pi + \mu Q_s \theta} \end{array} \right\} \cdot e^{j2\xi wt}$
Interaction of PM field with real part coefficient and imaginary part coefficient of slotting effect	$\mu Q_s - \xi p = 0$ $m \neq \mu$	2ξ	$-\frac{r_0^2 \cdot \lambda_{a\mu} \cdot \lambda_{b\mu}}{2\mu_0} \cdot \left\|B_{r,1}(\mathrm{r},\beta,z)^m\right\|^2 \cdot \frac{L}{2} \cdot \pi \cdot \sin(\mu Q_s \theta) \cdot \left[\begin{array}{l} \frac{1}{\mu Q_s \theta} + \frac{1}{2m\pi - 2\mu Q_s \theta} \\ -\frac{1}{2m\pi + 2\mu Q_s \theta} \end{array} \right] \cdot e^{j2\xi wt}$

B. Cogging Torque

Based on Maxwell's stress tensor in cylindrical coordinates, the cogging torque considering skewing can be written as

$$T_{\mathrm{cog}} = \frac{r_0^2}{\mu_0} \cdot \sum_{\xi} \sum_{m} \sum_{\mu} \int_{-\frac{L}{2}}^{\frac{L}{2}} \int_{-\pi}^{\pi} \mathrm{Re}\left\{ \begin{array}{l} \xi,m B_{\beta,1}(r,\beta,z)^m \\ \cdot^{\xi,m} B_{r,1}(r,\beta,z)^m \end{array} \right\} \mathrm{d}\alpha \, \mathrm{d}z. \tag{22}$$

Due to the low amplitude, the tangential air-gap flux density can be converted to the radial component multiplied by the imaginary part of the complex relative permeance function, and thus the cogging torque becomes

$$T_{\mathrm{cog}} = -\frac{r_0^2}{\mu_0} \cdot \sum_{\xi} \sum_{m} \sum_{\mu} \int_{-\frac{L}{2}}^{\frac{L}{2}} \int_{-\pi}^{\pi} \times \mathrm{Re}\left\{ \begin{array}{c} \left|B_{r,1}(r,\beta,z)^m\right|^2 \cdot \cos^2\left(m\frac{\pi}{L}z\right) \\ e^{2j(\xi\cdot w\cdot t - \xi\cdot\beta)} \cdot \lambda_a \cdot \lambda_b \end{array} \right\} \mathrm{d}\alpha \, \mathrm{d}z. \tag{23}$$

Equations (15)–(17) are substituted into (23), and the cogging torque transforms into (24), as shown at the bottom of the page. It should be noted that: the cogging torque consists of two sources. The first source is the interaction of the PM field with a real part constant and imaginary part coefficient of the slotting effect, and the other is the interaction of the PM field with real and imaginary part coefficients of the slotting effect. For the first source, as the example, the solution is as follows, which expression is

$$T_{\mathrm{cog}} = -\frac{r_0^2}{\mu_0} \cdot \sum_{\xi} \sum_{m} \sum_{\mu} \left\{ \begin{array}{l} \left|B_{r,1}(r,\beta,z)^m\right|^2 \cdot \lambda_{a0} \cdot \lambda_{b\mu} \cdot e^{2j\xi wt} \\ \cdot \int_{-\frac{L}{2}}^{\frac{L}{2}} \int_{-\pi}^{\pi} \left[\begin{array}{l} e^{-2j\xi p\alpha} \cdot \cos^2\left(m\frac{\pi}{L}z\right) \\ \cdot \sin\left[\mu Q_s\left(\alpha + \frac{z}{L}\theta\right)\right] \end{array} \right] \mathrm{d}\alpha \, \mathrm{d}z \end{array} \right\}. \tag{25}$$

The integral term in (25) is labeled Y, and its simplification process is shown in Appendix III. Then, the circumferential integral can be written as

$$\int_{-\pi}^{\pi} e^{-2j\xi\cdot p\cdot\alpha} \cdot e^{j\mu Q_s \alpha} \, \mathrm{d}\alpha = \int_{-\pi}^{\pi} e^{j(\mu Q_s - 2\xi\cdot p)\alpha} \, \mathrm{d}\alpha. \tag{26}$$

For $\mu Q_s - 2\xi p \neq 0$

$$\int_{-\pi}^{\pi} e^{j(\mu Q_s - 2\xi p)\alpha} \, \mathrm{d}\alpha = -\frac{j}{(\mu Q_s \pm 2\xi p)} e^{j(\mu Q_s - 2\xi p)\alpha}\Big|_{-\pi}^{\pi} = 0. \tag{27}$$

For $\mu Q_s - 2\xi p = 0$

$$\int_{-\pi}^{\pi} e^{j(\mu Q_s - 2\xi p)\alpha} \, \mathrm{d}\alpha = \int_{-\pi}^{\pi} \mathrm{d}\alpha = 2\pi. \tag{28}$$

Therefore, the circumferential harmonic related to PMs and the slotting effect needs to meet $\mu Q_s - 2\xi p = 0$.

For the axial integral, the expression can be written as

$$\begin{aligned} &\int_{-\frac{L}{2}}^{\frac{L}{2}} \left[\cos^2\left(m\frac{\pi}{L}z\right) \cdot \cos\left(\mu Q_s \frac{z}{L}\theta\right)\right] \mathrm{d}z \\ &\quad = \sin\left(\mu Q_s \frac{\theta}{2}\right) \cdot \frac{L}{2} \\ &\qquad \cdot \left\{ \frac{1}{\mu Q_s \frac{\theta}{2}} + \frac{1}{2m\pi - \mu Q_s \theta} - \frac{1}{2m\pi + \mu Q_s \theta} \right\}. \end{aligned} \tag{29}$$

To simplify the analysis, the axial condition needs to be assumed as follows: $m \neq \mu$. Meanwhile, according to the circumferential and axial integral, (25) is written as Table I, with source, circumferential/axial condition, frequency, and amplitude. The cogging torque is divided into two classes based on the source. In analogy, the second source is also denoted in Table I.

$$T_{\mathrm{cog}} = -\frac{r_0^2}{\mu_0} \cdot \sum_{\xi} \sum_{m} \sum_{\mu} \int_{-\frac{L}{2}}^{\frac{L}{2}} \int_{-\pi}^{\pi} \mathrm{Re}\left\{ \begin{array}{l} \left|B_{r,1}(r,\beta,z)^m\right|^2 \cdot e^{2j(\xi\cdot w\cdot t - \xi\cdot\beta)} \cdot \lambda_{a0} \cdot \lambda_{b\mu} \cdot \cos^2\left(m\frac{\pi}{L}z\right) \cdot \sin\left[\mu Q_s\left(\alpha + \frac{z}{L}\theta\right)\right] \\ +\left|B_{r,1}(r,\beta,z)^m\right| \cdot \frac{1}{2} \cdot e^{2j(\xi\cdot w\cdot t - \xi\cdot\beta)} \cdot \lambda_{a\mu} \cdot \lambda_{b\mu} \cdot \cos^2\left(m\frac{\pi}{L}z\right) \cdot \sin\left[2\mu Q_s\left(\alpha + \frac{z}{L}\theta\right)\right] \end{array} \right\} \mathrm{d}\alpha \, \mathrm{d}z \tag{24}$$

TABLE II
SOURCE, CIRCUMFERENTIAL CONDITION, FREQUENCY AND AMPLITUDE OF COGGING TORQUE WITHOUT CONSIDERING SKEWING

Source	Circumferential condition	Frequency	Amplitude
Interaction of PM field with real part constant and imaginary part coefficient of slotting effect	$\mu Q_s - 2\xi p = 0$	2ξ	$-\frac{r_0^2 \cdot \lambda_{a0} \cdot \lambda_{b\mu}}{2\mu_0} \cdot \left\lvert B_{r,1}(\mathrm{r},\beta,z)^m \right\rvert^2 \cdot L \cdot \pi \cdot e^{j2\xi wt}$
Interaction of PM field with real part coefficient and imaginary part coefficient of slotting effect	$\mu Q_s - \xi p = 0$	2ξ	$-\frac{r_0^2 \cdot \lambda_{a\mu} \cdot \lambda_{b\mu}}{2\mu_0} \cdot \left\lvert B_{r,1}(\mathrm{r},\beta,z)^m \right\rvert^2 \cdot \frac{L}{2} \cdot \pi \cdot e^{j2\xi wt}$

Setting $\theta = 0$, i.e., no skewing, the expression of cogging torque in Table I can be transformed into that in Table II. Comparing the cogging torque in Tables I and II, we can get: 1) The different point is the amplitude, i.e., only the value of cogging torque is modulated by the skew effect, which is caused by differences in axial integral. Here, the difference between the axial integral with and without considering skewing is called the skewing factor, which is related to the skew angle, the number of slots, and poles. Moreover, the amplitude of cogging torque is proportional to the skewing factor. Since the function of the skewing factor is a decreasing function, the skew effect becomes prominent with the skew angle enhancement. In the extreme case, the amplitude of cogging torque is modulated to zero by setting $\theta = 2\pi/Q_s$. 2) The constant points are the source and period of cogging torque.

For the axial harmonics, the effect is mainly reflected in ${}^m a$ and skewing factor. Then, the axial harmonic only affects the value of the skewing factor, i.e., the axial harmonic cannot reduce the ability of certain circumferential harmonic of slotting effect, which can be eliminated by the skewing.

According to the expression of cogging torque, the mechanical period of the cogging torque is obtained as

$$C_{\mathrm{cog}} = \frac{2\pi}{2p\xi}. \tag{30}$$

For the value of ξ, the circumferential condition in the first source needs to meet $\mu Q_s - 2\xi p = 0$. Meanwhile, ξ is also an integer, and thus the value of ξ is

$$\xi = \mu \frac{Q_s}{2p} = \varsigma \frac{Q_s}{\mathrm{GCD}(2p,\, Q_s)}, \quad \varsigma = 1, 2, 3, \ldots \tag{31}$$

where $\mathrm{GCD}(2p,\ Q_s)$ is the greatest common divisor of $2p$ and Q_s.

In analogy, the value of ξ should be met in the second source

$$\xi = \mu \frac{Q_s}{p} = \varsigma \frac{Q_s}{\mathrm{GCD}(p,\, Q_s)}. \tag{32}$$

In summary, the value of ξ is

$$\xi = \mu \frac{Q_s}{2p} = \varsigma \frac{Q_s}{\mathrm{GCD}(2p,\, Q_s)}. \tag{33}$$

Referring to (30), the period of cogging torque is

$$C_{\mathrm{cog}} = \frac{2\pi \cdot \mathrm{GCD}(2p,\, Q_s)}{2pQ_s} = \frac{2\pi}{\mathrm{LCM}(2p,\, Q_s)} \tag{34}$$

where $\mathrm{LCM}(2p,\ Q_s)$ is the least common multiple of $2p$ and Q_s.

C. Flux Linkage Due to PMs

To calculate the flux linkage excited by PMs, a calculation for the κth coil of the ρth pole group of the kth phase is needed. Meanwhile, in order to consider the end effect in the z-direction, the winding distribution should be considered by ${}^n b \cdot \cos(n\pi z/L_z)$. Therefore, the flux linkage considering skewing can be expressed as

$$\psi = -N_c \sum_{\mu} \sum_{n} \sum_{m} \sum_{\xi} \int_{-\frac{L}{2}}^{\frac{L}{2}} \int_{-\frac{\pi}{2}\frac{y}{\tau_p}}^{\frac{\pi}{2}\frac{y}{\tau_p}} \left[{}^n b \cdot \cos\left(n\frac{\pi}{L_Z} z\right) \cdot {}^{\xi,m} B_{r,1}(r,\beta,z)^m \right] \cdot \lambda_a \cdot r_0 \cdot \mathrm{d}\beta\, \mathrm{d}z. \tag{35}$$

By summing up the flux linkage of all q coils per coil group and all $2p$ coil groups per phase gives the factor $2pq \cdot {}^{\nu}\xi_z$. Then, the flux linkage of the kth phase considering skewing can be written as

$$\psi = -W \sum_{\mu} \sum_{n} \sum_{m} \sum_{\xi} {}^{\upsilon}\xi_z \cdot \int_{-\frac{L}{2}}^{\frac{L}{2}} \int_{-\frac{\pi}{2}\frac{y}{\tau_p}}^{\frac{\pi}{2}\frac{y}{\tau_p}} \left[{}^n b \cdot \cos\left(n\frac{\pi}{L_Z} z\right) \cdot {}^{\xi,m} B_{r,1}(r,\beta,z)^m \right] \cdot \lambda_a \cdot r_0 \cdot \mathrm{d}\beta\, \mathrm{d}z. \tag{36}$$

In analogy with Section III-B, the resultant flux linkage of the kth phase considering skewing is shown in Table III, which can also be divided into a couple of classes based on the source. As to the source, the first source is that the interaction of the PM field with real part constant of slotting effect, and the second source is the interaction of the PM field with real part coefficient of slotting effect. Setting $\theta = 0$, i.e., no skewing, the expression of the flux linkage of the kth phase can be classified in Table IV.

For the circumferential integral of the first source, as the example, the expression is as follows:

$$\int_{-\frac{\pi}{2}\frac{y}{\tau_p}}^{\frac{\pi}{2}\frac{y}{\tau_p}} e^{-j\xi\beta}\, \mathrm{d}\beta = \frac{2}{\xi} \cdot \sin\left(\xi \frac{\pi}{2} \frac{y}{\tau_p}\right). \tag{37}$$

Based on (37), the value of full pitch is $\xi/2$. However, as to the short pitch, the value of the circumferential integral is less than $\xi/2$, which means the short pitch is an effective method to suppress back EMF.

Comparing Tables III and IV, we can get: 1) The first source is constant, but the second source is modulated by the skew effect. Here, the function of the skew factor is consistent with

TABLE III
SOURCE AND AMPLITUDE OF FLUX LINKAGE CONSIDERING SKEWING

Source	axial condition	Frequency	Amplitude
Interaction of PM field with real part constant of slotting effect	$n = m$	ξ	$-\lambda_0 \cdot W \cdot {}^{n}b \cdot {}^{v}\xi_z \cdot L \cdot \frac{r_0 \cdot B_{r,1}^{m}}{\xi} \cdot \sin(\xi \frac{\pi}{2} \frac{y}{\tau_p}) \cdot e^{j\xi wt}$
Interaction of PM field with real part coefficient of slotting effect	$n = m$	ξ	$-\left[\lambda_{a\mu} \cdot W \cdot {}^{n}b \cdot p \cdot {}^{v}\xi_z \cdot L \cdot \frac{r_0 \cdot B_{r,1}^{m}}{2}\right] \sin(\mu Q_s \frac{\theta}{2}) \cdot \left\{\frac{1}{\mu Q_s \frac{\theta}{2}} + \frac{1}{2m\pi - \mu Q_s \theta} - \frac{1}{2m\pi + \mu Q_s \theta}\right\} \cdot \left\{\frac{\sin\left[(\xi + \mu Q_S/p)\frac{\pi}{2}\frac{y}{\tau_p}\right]}{p\xi + \mu Q_S} + \frac{\sin\left[(\xi - \mu Q_S/p)\frac{\pi}{2}\frac{y}{\tau_p}\right]}{p\xi - \mu Q_S}\right\} \cdot e^{j\xi wt}$

TABLE IV
SOURCE AND AMPLITUDE OF FLUX LINKAGE WITHOUT CONSIDERING SKEWING

Source	axial condition	Frequency	Amplitude
Interaction of PM field with real part constant of stator slotting	$n = m$	ξ	$-\lambda_0 \cdot W \cdot {}^{n}b \cdot {}^{v}\xi_z \cdot L \cdot \frac{r_0 \cdot B_{r,1}^{m}}{\xi} \cdot \sin(\xi \frac{\pi}{2} \frac{y}{\tau_p}) \cdot e^{j\xi wt}$
Interaction of PM field with real part coefficient of stator slotting	$n = m$	ξ	$-\left[\lambda_{a\mu} \cdot W \cdot {}^{n}b \cdot {}^{v}\xi_z \cdot L \cdot \frac{r_0 \cdot B_{r,1}^{m}}{2} \cdot p\right] \cdot \left\{\frac{\sin\left[(p\xi + \mu Q_S/p)\frac{\pi}{2}\frac{y}{\tau_p}\right]}{p\xi + \mu Q_S} + \frac{\sin\left[(p\xi - \mu Q_S/p)\frac{\pi}{2}\frac{y}{\tau_p}\right]}{p\xi - \mu Q_S}\right\} \cdot e^{j\xi wt}$

that of cogging torque. Therefore, the effect of sinusoidal back EMF is proportional to the skew angle. However, the higher amplitude of the first source and only the second source modulated by the skew effect make the flux linkage of kth phase partially weaken. 2) The axial condition and period are not affected by the skew effect.

IV. SIMULATION AND DISCUSSION

In order to validate the modulation principle of the skew effect on the air-gap flux density, cogging torque, and back EMF, the basic parameters of the SPM machine are given in Table V.

TABLE V
SPM PARAMETER OVERVIEW

Parameter	Value	Parameter	Value
Number of poles	4	Number of slot	24
Thickness of PMs	4mm	Turns per coil	3
Coils per phase	4	Air gap length	1mm
Connection group of windings	Wye	Skewed slot	One slot pitch
Outer radius of stator core	140mm	Inner radius of stator core	88mm
Axial length	88mm	Maximum speed	3200rpm
Magnetizing direction	radial		

A. Air-Gap Flux Density

Under different axial positions, the air-gap flux density excited by each magnetic excitation is shown in Fig. 7, respectively. Each case shows an identical rotor position. Obviously, the waveforms calculated by the analytical model can match well with that of FEM in each magnetic field. Meanwhile, the features of each case are as follows. As to the air-gap flux density of winding current, step shape is the prominent feature, which is caused by the distributed winding. As the axial position changes, the air-gap flux density distribution integrally moves along the circumferential direction. This is because the MMF of current and the slotting effect are affected by the skew effect.

As to the air-gap flux density of PMs, the distribution is featured by square waves.

1) As to overview, the distribution keeps constant under different axial positions, i.e., the nonslotted flux density distribution is unchanged.
2) Specifically for a unit, the circumferential position of mutation caused by the slotting effect varies with the axial position changes.

This is because only the slotting effect is affected by the skew effect in this case.

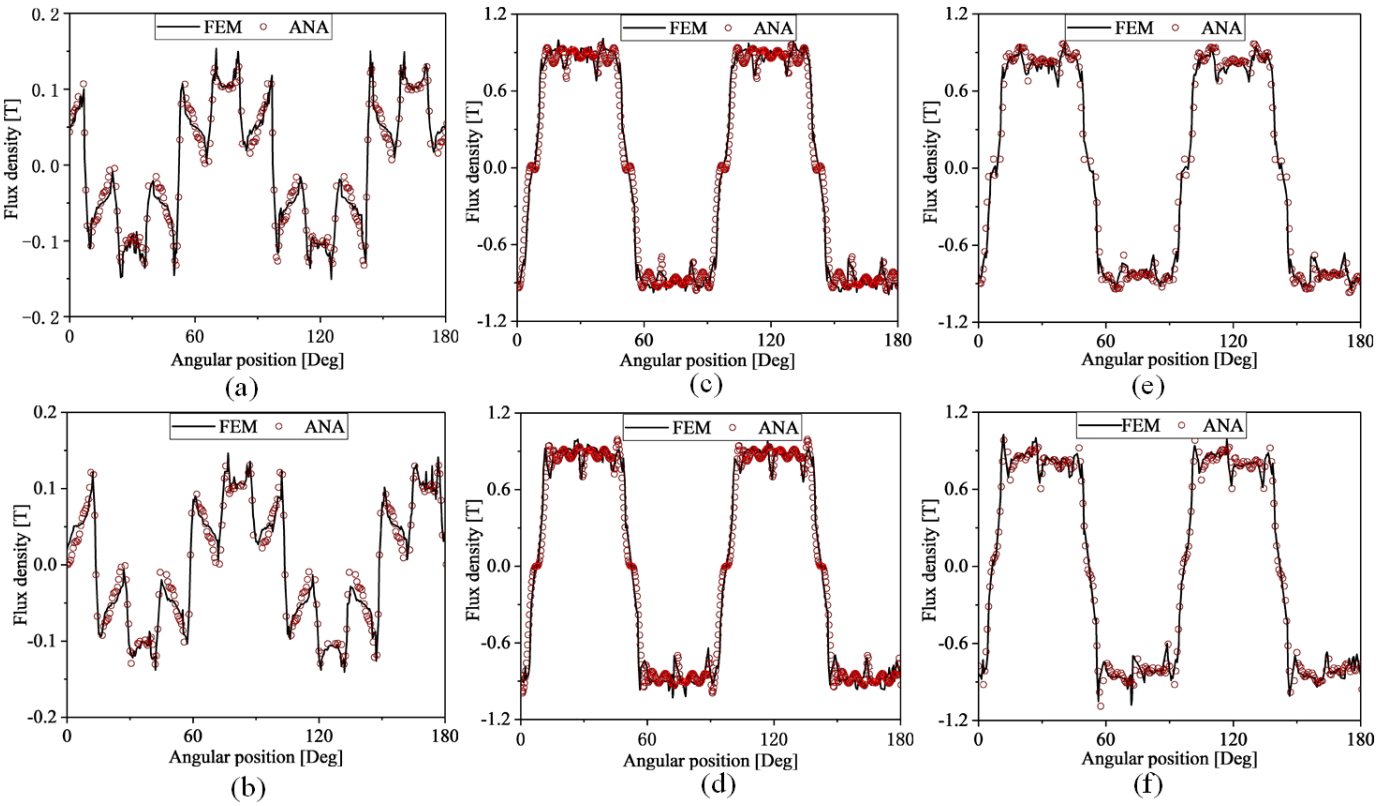

Fig. 7. Air-gap flux density under different axial positions. (a) Flux density of current under $z = 0$. (b) Flux density of current under $z = 35$ mm. (c) Flux density of PM under $z = 0$. (d) Flux density of PM under $z = 35$ mm. (e) Flux density of joint excitation under $z = 0$. (f) Flux density of joint excitation under $z = 35$ mm.

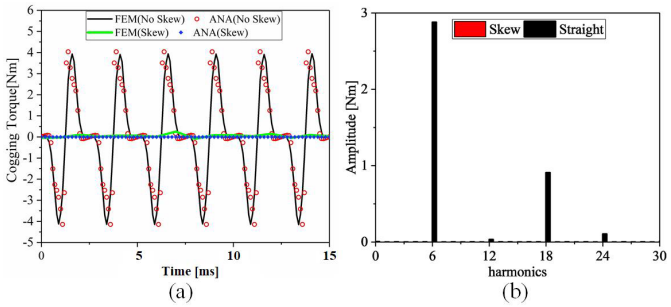

Fig. 8. Cogging torque and FFT. (a) Cogging torque. (b) FFT.

As to the joint excitation, a similar square-like distribution is presented, which is caused by the higher amplitude of flux density of PMs. Compared with only PMs excitation, different points are listed as follows: (1) lower amplitude and (2) higher distortion. The reason is that the winding current presents demagnetization under motor mode.

B. Cogging Torque

Under the 1000 r/min, cogging torques of a couple of skew angles are shown in Fig. 8(a). Transient FE works as a reference. Obviously, the agreement between both methods is shown. For the cogging torque without considering skewing, according to (34), the period is $2\pi/Q_s$. This is because the value of LCM($2p$, Q_s) is equal to Q_s. At 1000 r/min, the time required for one mechanical revolution is 60 ms. In Fig. 8(a), 15 ms is a quarter cycle; that is, the period is $2\pi/Q_s$, which is consistent with the theoretical analysis. To conduct mechanism studies on the skew effect, setting $\theta = 2\pi/Q_s$. The value of cogging torque is almost equal to zero. This is because the value of $\sin(\mu Q_s\theta/2)$ and $\sin(\mu Q_s\theta)$ is equal to zero, i.e., the value of skewing factor is zero.

The corresponding FFT of cogging torques of a couple of skew angles is shown in Fig. 8(b). We can get: 1) The same point is that the order of frequency harmonics is the multiple of 6. Since the value of GCD($2p$, Q_s) is equal to $2p$, and thus the value of ξ is equal to 3ς. Meanwhile, the order of frequency is 2ξ. 2) The values of each harmonic are almost 0 when the skew angle is $2\pi/Q_s$.

Since the value of cogging torque is proportional to the skewing factor, the accuracy of the analytical model is dependent on the calculated skewing factor. According to Fig. 8(b), the main harmonic orders of cogging torque without considered skewing are the 6th and the 18th, i.e., $\mu = 1, 3$. Therefore, under the condition of $\mu = 1, 3$, the value of the skewing factor is studied.

For the fundamental order of circumferential harmonic, under several typical skew angles, values of the skewing factor calculated by the analytical method and FEM are shown in Fig. 9(a). It should be noted that the value of x-axial is $Q_s \cdot \theta/\pi$. Meanwhile, the features of the skewing factor are as follows.

1) The value of skewing factor presents a downward trend as the skew angle enlarges, which is consistent with the theoretical analysis.

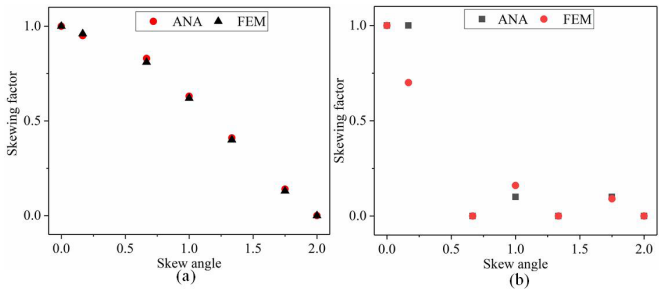

Fig. 9. Value of skewing factor. (a) Fundamental harmonic. (b) Third order.

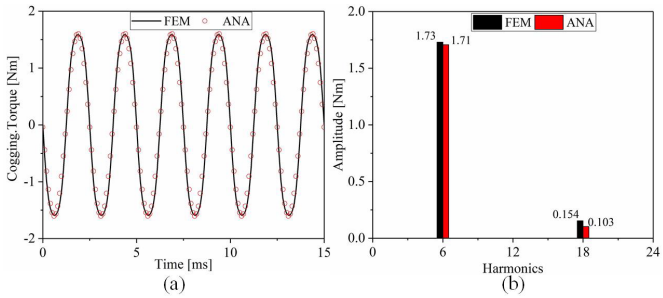

Fig. 10. Cogging torque and FFT under arbitrary skew angle. (a) Cogging torque. (b) FFT.

2) The value of the analytical method is consistent with that of FEM in different skew angles.
3) The value of the skew angle needs to be set $2\pi/Q_s$ to maximum suppression of cogging torque.

For the third order of circumferential harmonic, under the same setting condition of fundamental harmonic, the value of skewing factor calculated by analytical method and FEM is shown in Fig. 9(b). We can get: 1) When the skew angle is small, the value of the analytical method is larger than that of FEM. The reason is that the value of the skewing factor is mainly $\sin(\mu Q_s(\theta/2))/\mu Q_s(\theta/2)$ and $\sin(\mu Q_s(\theta/2))/2m\pi - \mu Q_s\theta$, which is caused by that the higher value of $2m\pi + \mu Q_s\theta$. As to the third order, the axial harmonic of PMs is mainly considered the fundamental order, i.e., $m = 1$. Meanwhile, the value of $2m\pi - \mu Q_s\theta$ is relatively low in this case, which leads to the value of $\sin(\mu Q_s(\theta/2))/2m\pi - \mu Q_s\theta$ is correspondingly large. However, the value of $\sin(\mu Q_s(\theta/2))/\mu Q_s(\theta/2)$ is almost close to the result of FEM. Therefore, the axial harmonic of PMs has a significant effect. 2) When the skew angle is larger, the result of the analytical method matches well with that of FEM. As the overview, the value of the 18th harmonic of cogging torque is smaller, and thus the axial harmonic has little effect on the total value of cogging torque.

Further, to validate the modulation theory of the skew effect on cogging torque, the arbitrary skew angles are investigated. Setting $\theta = \pi/Q_s$, the corresponding cogging torque and FFT calculated by the analytical model and FEM are shown in Fig. 10. Besides, the analytical model is in good agreement with FEM. Compared with cogging torque without considering skewing, we can get: 1) The amplitudes of each harmonic become smaller. This is because the skewing factor is a decreasing function, and the value of cogging torque is modulated by the skewing factor. 2) The waveform presents sinusoidal. The reason is that the amplitude of the 18th harmonic is quite small, which is caused by the skew effect. As to FFT of cogging torque, the amplitude of the 6th harmonic is basically the same, and the amplitude of the 18th harmonic is a little smaller, which is consistent with the theory of the skewing factor. In a word, at different skew angles, the cogging torque considering the skewing of the analytical model is consistent with that of FEM.

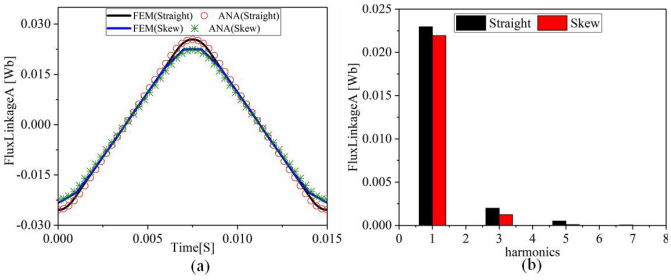

Fig. 11. Flux linkage and FFT. (a) Flux linkage of A-phase winding. (b) FFT.

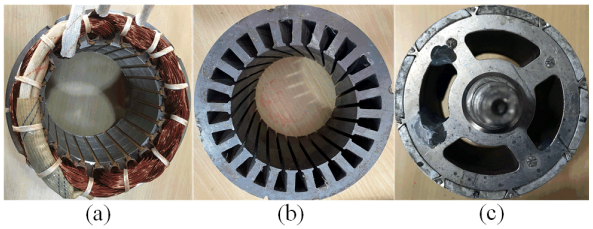

Fig. 12. Prototype. (a) Stator with straight slots. (b) Stator with skewed slots. (c) Rotor.

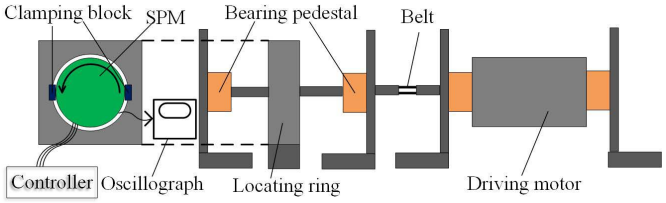

Fig. 13. Schema of the test bench.

C. Flux Linkage Due to PMs

The flux linkage of A-phase winding and FFT are shown in Fig. 11. It should be noted that skewing is considered by setting $\theta = 2\pi/Q_s$. The features of flux linkage are as follows.

1) As to overview, the fundamental order is working harmonic, and third is the main undesired harmonic. This is because the frequency order is ξ, and the amplitude of ξ is positive odd numbers.
2) As to the SPM with skewed slots, the amplitude of the fundamental order is slightly reduced, which is caused by the weakening of the amplitude of the flux linkage generated by the second source. However, the amplitude of the flux linkage generated by the first source occupies

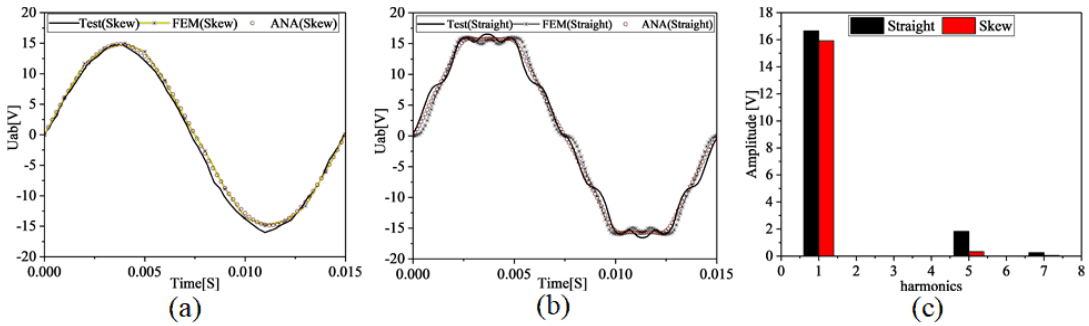

Fig. 14. Back EMF and FFT. (a) SPM with skewed slots. (b) SPM with straight slots. (c) FFT.

the vast majority of the overall flux, which does not change with skewed slots.

3) The analytical method can well match the FEM.

V. Experimental Verification

In this section, the SPM machines with straight and skewed slots are manufactured to validate the theoretical analysis and FEM results, which are shown in Fig. 12. The only difference between two prototypes is the stator in the mechanical structure.

Hence, in order to measure the back EMF, the experimental setup is shown in Fig. 13, including a driving motor, an SPM machine, and a digital oscilloscope. Here, the appearance of the controller is to illustrate that the SPM system consists of the motor and controller. Hence, the controller does not participate during the experiment of the back EMF. Meanwhile, the SPM machine is the tested motor, the induction motor is the driving motor, and they are linked together by a belt. The digital oscilloscope is utilized to save the waveform and data of back EMF. The tested SPM is driven by the driving motor at the speed (1000 r/min). The line back EMF waveforms for both machines are recorded and exhibited in Fig. 14.

The line back EMF results of the SPM machines with skewed and straight slots at 1000 r/min are shown in Fig. 14(a) and (b). It is shown as follows.

1) As to overview, the fundamental order is an effective harmonic, the fifth is the main harmful harmonic, and the amplitude of third harmonic is zero, which is caused by the connection group of windings.
2) As to the SPM machine with skewed slots, the fundamental order of the line back EMF is slightly decreased because the fundamental order of flux linkage is weakened, and the back EMF is the derivative of the flux linkage to time.
3) The waveform of the back EMF of the SPM with skewed slots is more sinusoidal because the fifth harmonics are greatly suppressed.
4) The analytical method can well match FEM and experimental waveforms.

VI. Conclusion

In this article, Maxwell's equations-based 3-D analytical model is utilized to study the mechanism that the cogging torque, flux linkage, and back EMF are modulated by the skew effect. By the comparative study of the motors with straight and skewed slots, the differences in the electromagnetic field are shown. For the 3-D air-gap flux density, the features are as follows.

1) As to only current excitation, the step-like distribution translates in the circumferential direction as the axial position changes.
2) As to only PM excitation, the unchanged square-like distribution, and alterable mutation.
3) As to the joint excitation, the same square-like distribution with characteristics of lower amplitude and higher distortion.

Based on the difference in electromagnetic characteristics, the modulation principle of the skew effect is obtained. As to cogging torque, the amplitudes of two sources are modulated by the skew effect, but the period is not affected. Further, the amplitude of cogging torque considering skewing is proportional to the skewing factor, which is calculated by comparing cogging torque with and without considering skewing. Meanwhile, the skewing factor is a decreasing function, which results in setting $\theta = 2\pi/Q_s$ to maximize the suppression of the cogging torque. As to the back EMF, only the amplitude of the second source is modulated by the skew effect. Meanwhile, under different skew angles, the first source keeps constant and has a higher value, which makes the machine consider skewing more sinusoidal rather than eliminated. Finally, the validity of the analytical model is verified by the experiment.

Hence, the 3-D analytical model has proven to study well the modulation principle of skew effect on electromagnetic characteristics.

Appendix I

For only current excitation, Maxwell's equations are solved by the separation method, starting from the first layer [22], and Poisson's equation is transformed into the homogeneous modified Bessel's equation. Then, these constants can be calculated based on boundary conditions, which are expressed as (A-1)–(A-5), shown at the bottom of the next page.

Therefore, the magnetic vector potential of the air-gap can be expressed as

$$
\begin{aligned}
{}^{v,n}A^{S}_{z,1} = {}& {}^{v,n}C^{S}_{5}\left(I_{v_p}\left({}^{n}k_1 r\right) + {}^{v,n}C^{S}_{6}K_{v_p}\left({}^{n}k_1 r\right)\right) \\
& \cdot {}^{n}b\cos\left(n\frac{\pi}{L_z}z\right)e^{j\left[wt-\frac{v}{p}\left(\beta-p\frac{z}{L}\cdot\theta\right)\right]}
\end{aligned}
$$

$$ {}^{\upsilon,n}A^{S}_{\beta,1} = j\frac{r}{\upsilon_p}\frac{n\pi}{L_z}\cdot {}^{\upsilon,n}C^{S}_{5}\left(I_{\upsilon_p}\left({}^{n}k_1 r\right) + {}^{\upsilon,n}C^{S}_{6}K_{\upsilon_p}\left({}^{n}k_1 r\right)\right) \cdot {}^{n}b\sin\left(n\frac{\pi}{L_z}z\right)e^{j\left[\omega t-\frac{n}{p}\left(\beta-p\frac{z}{L}\cdot\theta\right)\right]}. \tag{A-6} $$

APPENDIX II

For only PM excitation, compared with the solving process of Maxwell's equations under only current excitation, the difference in PMs layer is because of the magnetization. The separation of variables method is also used, but Poisson's equation is transformed into the inhomogeneous modified Bessel's equation. Then, constants can be calculated by boundary conditions (B-1) and (B-2), as shown at the bottom of the page.

With (B-3) and (B-4), as shown at the bottom of the page. With

$$ \begin{aligned} A(3,2) &= I_{\xi-1}(k_3\cdot r_2) + I_{\xi+1}(k_3\cdot r_2)\\ B(2,2) &= K_{\xi-1}(k_2\cdot r_2) + K_{\xi+1}(k_2\cdot r_2)\\ A(2,2) &= I_{\xi-1}(k_2\cdot r_2) + I_{\xi+1}(k_2\cdot r_2) \end{aligned} \tag{B-5} $$

$$ {}^{\xi,m}C^{m}_{9} = -j\frac{\mu_0{}^{\xi}M^{\Delta}\left[{}^{\xi,m}C^{m}_{7}\cdot I_{\xi}(k_2\cdot r_2) + {}^{\xi,m}C^{m}_{8}\cdot K_{\xi}(k_2\cdot r_2) + R_{2P}\right]}{I_{\xi}(k_3\cdot r_2)} \tag{B-6} $$

$$ {}^{\xi,m}C^{m}_{5} = -j\frac{\mu_0{}^{\xi}M^{\Delta}\cdot\left[{}^{\xi,m}C^{m}_{7}\cdot I_{\xi}(k_2\cdot r_1) + {}^{\xi,m}C^{m}_{8}\cdot k_{\xi}(k_2\cdot r_1) + R_{2P}\right]}{I_{\xi}(k_1\cdot r_1) + {}^{\xi,m}C^{m}_{6}\cdot K_{\xi}(k_1\cdot r_1)} \tag{B-7} $$

where R_{2p} is the particular solution of the inhomogeneous modified Bessel's equation. For different orders, the particular solution has different expressions, but it can be derived as follows.

For $\xi = 1$

$$ {}^{\xi,m}R_{2P} = -\frac{1}{{}^{m}k_2}\begin{bmatrix} I_1\left({}^{m}k_2\cdot r\right)\cdot K_0\left({}^{m}k_2\cdot r\right)\\ +K_1\left({}^{m}k_2\cdot r\right)\cdot I_0\left({}^{m}k_2\cdot r\right)\end{bmatrix}. \tag{B-8} $$

For $\xi = 3, 5, 7, \ldots$ (B-9), as shown at the top of the next page.

Therefore, the magnetic vector potential of the air-gap can be expressed as

$$ {}^{\xi,m}A^{m}_{z,1} = {}^{\xi,m}C^{m}_{5}\left[I_{\xi}\left({}^{\kappa}k_1\cdot r\right) + {}^{\xi,\kappa}C^{m}_{6}\cdot K_{\xi}\left({}^{m}k_1\cdot r\right)\right] \cdot {}^{m}a\cdot\cos\left(m\frac{\pi}{L}z\right)\cdot e^{j(\xi\omega t-\xi\beta)} $$

$$ {}^{\upsilon,n}C^{S}_{5} = -j\mu_1\frac{N_{\mathrm{ph}}}{\pi r_0}W^{\upsilon}\xi_z\cdot{}^{\upsilon}\xi_s\cdot{}^{\upsilon}\xi_N\cdot\sqrt{2}\ I\cdot\frac{2\mu_1/{}^{n}k_1}{{}^{n}k_1\left(I_{\upsilon_p-1}({}^{n}k_1 r_0) + I_{\upsilon_p+1}({}^{n}k_1 r_0) - {}^{\upsilon,n}C^{S}_{6}\left(K_{\upsilon_p-1}({}^{n}k_1 r_0) + K_{\upsilon_p+1}({}^{n}k_1 r_0)\right)\right)} \tag{A-1} $$

$$ {}^{\upsilon,n}C^{S}_{6} = -\frac{I_{\upsilon_p}({}^{n}k_1 r_1) - \left[I_{\upsilon_p-1}({}^{n}k_1 r_1) + I_{\upsilon_p+1}({}^{n}k_1 r_1)\right]\frac{{}^{n}k_1}{{}^{n}k_2}\frac{\mu_2}{\mu_1}\frac{I_{\upsilon p}({}^{n}k_2 r_1)+{}^{\upsilon,n}C^{S}_{8}K_{\upsilon p}({}^{n}k_2 r_1)}{I_{\upsilon p-1}({}^{n}k_2 r_1)+I_{\upsilon p+1}({}^{n}k_2 r_1)-{}^{\upsilon,n}C^{S}_{8}\left[K_{\upsilon p-1}({}^{n}k_2 r_1)+K_{\upsilon p+1}({}^{n}k_2 r_1)\right]}}{K_{\upsilon_p}({}^{n}k_1 r_1) + \left[K_{\upsilon_p-1}({}^{n}k_1 r_1) + K_{\upsilon_p+1}({}^{n}k_1 r_1)\right]\frac{{}^{n}k_1}{{}^{n}k_2}\frac{\mu_2}{\mu_1}\frac{I_{\upsilon p}({}^{n}k_2 r_1)+{}^{\upsilon,n}C^{S}_{8}K_{\upsilon p}({}^{n}k_2 r_1)}{I_{\upsilon p-1}({}^{n}k_2 r_1)+I_{\upsilon p+1}({}^{n}k_2 r_1)-{}^{\upsilon,n}C^{S}_{8}\left[K_{\upsilon p-1}({}^{n}k_2 r_1)+K_{\upsilon p+1}({}^{n}k_2 r_1)\right]}} \tag{A-2} $$

$$ {}^{\upsilon,n}C^{S}_{8} = -\frac{I_{\upsilon_p}({}^{n}k_2 r_2) - \left[I_{\upsilon_p-1}({}^{n}k_2 r_2) + I_{\upsilon_p+1}({}^{n}k_2 r_2)\right]\cdot\frac{{}^{n}k_2}{{}^{n}k_3}\frac{\mu_3}{\mu_2}\frac{I_{\upsilon p}({}^{n}k_3 r_2)}{I_{\upsilon p-1}({}^{n}k_3 r_2)+I_{\upsilon p+1}({}^{n}k_3 r_2)}}{K_{\upsilon_p}({}^{n}k_2 r_2) + \left[K_{\upsilon_p-1}({}^{n}k_2 r_2) + K_{\upsilon_p+1}({}^{n}k_2 r_2)\right]\cdot\frac{{}^{n}k_2}{{}^{n}k_3}\frac{\mu_3}{\mu_2}\frac{I_{\upsilon p}({}^{n}k_3 r_2)}{I_{\upsilon p-1}({}^{n}k_3 r_2)+I_{\upsilon p+1}({}^{n}k_3 r_2)}} \tag{A-3} $$

$$ {}^{\upsilon,n}C^{S}_{7} = {}^{\upsilon,n}C^{S}_{6}\frac{I_{\upsilon_p}({}^{n}k_1 r_1) + {}^{\upsilon,n}C^{S}_{6}K_{\upsilon_p}({}^{n}k_1 r_1)}{I_{\upsilon_p}({}^{n}k_2 r_1) + {}^{\upsilon,n}C^{S}_{8}K_{\upsilon_p}({}^{n}k_2 r_1)} \tag{A-4} $$

$$ {}^{\upsilon,n}C^{S}_{9} = {}^{\upsilon,n}C^{S}_{7}\frac{I_{\upsilon_p}({}^{n}k_2 r_2) + {}^{\upsilon,n}C^{S}_{8}K_{\upsilon_p}({}^{n}k_2 r_2)}{I_{\upsilon_p}({}^{n}k_3 r_2)} \tag{A-5} $$

$$ {}^{\xi,m}C^{m}_{6} = \frac{I_{\xi-1}\left({}^{m}k_1\cdot r_0\right) + I_{\xi+1}\left({}^{m}k_1\cdot r_0\right)}{K_{\xi-1}\left({}^{m}k_1\cdot r_0\right) + K_{\xi+1}\left({}^{m}k_1\cdot r_0\right)} \tag{B-1} $$

$$ {}^{\xi,m}C^{m}_{7} = \frac{{}^{\xi,m}C_{8}\left\{\begin{matrix} K_{\xi}\left({}^{m}k_2\cdot r_1\right)\cdot D(k_1\cdot r_1)\\ +\frac{k_2}{k_1}\frac{\mu_1}{\mu_2}\begin{bmatrix} I_{\xi-1}\left({}^{m}k_2\cdot r_1\right)\\ +I_{\xi+1}\left({}^{m}k_2\cdot r_1\right)\end{bmatrix}\cdot G(k_1\cdot r_1)\end{matrix}\right\} + R_{3P}\left({}^{m}k_2\cdot r_1\right)\cdot D(k_1\cdot r_1) - \frac{k_2}{k_1}\frac{\mu_1}{\mu_2}\frac{2}{k_2}R'_{3P}\left({}^{m}k_2\cdot r_1\right)\cdot G(k_1\cdot r_1)}{\frac{k_2}{k_1}\frac{\mu_1}{\mu_2}\left[I_{\xi-1}\left({}^{m}k_2\cdot r_1\right) + I_{\xi+1}\left({}^{m}k_2\cdot r_1\right)\cdot G(k_1\cdot r_1)\right] - D(k_1\cdot r_1)\cdot I_{\xi}\left({}^{m}k_2\cdot r_1\right)} \tag{B-2} $$

$$ \begin{cases} D(k_1\cdot r_1) = \left[I_{\xi-1}\left({}^{m}k_1\cdot r_1\right) + I_{\xi+1}\left({}^{m}k_1\cdot r_1\right)\right] - {}^{\xi,m}C^{m}_{6}\cdot\left[K_{\xi-1}\left({}^{m}k_1\cdot r_1\right) + K_{\xi+1}\left({}^{m}k_1\cdot r_1\right)\right]\\ G(k_1\cdot r_1) = I_{\xi}\left({}^{m}k_1\cdot r_1\right) + {}^{\xi,m}C^{m}_{6}\cdot K_{\xi}\left({}^{m}k_1\cdot r_1\right)\end{cases} \tag{B-3} $$

$$ {}^{\xi,m}C^{m}_{8} = \frac{\begin{matrix}\left[\frac{k_2}{k_1}\frac{\mu_1}{\mu_2}\frac{2}{k_2}R'_{3P}\cdot G(1,1) + R_{3P}\cdot D(1,1)\right]\cdot\left[\frac{k_2}{k_3}\frac{\mu_3}{\mu_2}A(2,2)\cdot I_{\xi}(k_3\cdot r_2) - I_{\xi}(k_2\cdot r_2)\cdot A(3,2)\right]\\ +\left[-\frac{k_2}{k_3}\frac{\mu_3}{\mu_2}\frac{2}{k_3}R'_{3P} + R_{3P}\cdot A(3,2)\right]\cdot\left[\frac{k_2}{k_1}\frac{\mu_1}{\mu_2}\cdot A(2,1)\cdot G(1,1) - I_{\xi}(k_2\cdot r_1)\cdot D(1,1)\right]\end{matrix}}{\begin{matrix}\left[K_{\xi}(k_2\cdot r_1)\cdot D(1,1) + \frac{k_2}{k_1}\frac{\mu_1}{\mu_2}\cdot A(2,1)\cdot G(1,1)\right]\cdot\left[\frac{k_2}{k_3}\frac{\mu_3}{\mu_2}A(2,2)\cdot I_{\xi}(k_3\cdot r_2) - I_{\xi}(k_2\cdot r_2)\cdot A(3,2)\right]\\ -\left[I_{\xi}(k_2\cdot r_2)\cdot A(3,2) + \frac{k_2}{k_3}\frac{\mu_3}{\mu_2}\cdot B(2,1)\cdot I_{\xi}(k_3\cdot r_2)\right]\cdot\left[\frac{k_2}{k_1}\frac{\mu_1}{\mu_2}\cdot A(2,1)\cdot G(1,1) - I_{\xi}(k_2\cdot r_1)\cdot D(1,1)\right]\end{matrix}} \tag{B-4} $$

$$ {}^{\xi,m}R_{2P} = -\frac{1}{{}^{m}k_2}\left\{\begin{array}{l} I_\xi\left({}^{m}k_2\cdot r\right)\cdot\left[2\sum\limits_{n=0}^{(\xi-3)/2}(-1)^{n+1}\cdot K_{\xi-2n-1}({}^{m}k_2\cdot r)+(-1)^{(\xi-3)/2}\cdot K_0\left({}^{m}k_2\cdot r\right)\right] \\ -K_\xi\left({}^{m}k_2\cdot r\right)\cdot\left[2\sum\limits_{n=0}^{(\xi-3)/2}(-1)^{n}\cdot I_{\xi-2n-1}({}^{m}k_2\cdot r)+(-1)^{(\xi-1)/2}\cdot I_0\left({}^{m}k_2\cdot r\right)\right] \end{array}\right\} \tag{B-9} $$

$$ {}^{\xi,m}A^{S}_{\beta,1} = j\frac{r}{\xi}\frac{\kappa\pi}{L}\cdot{}^{\xi,m}C_5\left[I_\xi({}^{\kappa}k_1\cdot r)+{}^{\xi,m}C_6\cdot K_\xi\left({}^{m}k_1\cdot r\right)\right] \cdot{}^{m}a\sin\left(m\frac{\pi}{L}z\right)\cdot e^{j(\xi\omega t-\xi\beta)}. \tag{B-10} $$

Appendix III

The label Y can be written as

$$ \begin{aligned} Y &= \int_{-\frac{L}{2}}^{\frac{L}{2}}\int_{-\pi}^{\pi}\left[e^{2j\xi p\alpha}\cdot\cos^2\left(m\frac{\pi}{L}z\right)\cdot\sin\left[\mu Q_s\left(\alpha+\frac{z}{L}\theta\right)\right]\right]\mathrm{d}\alpha\,\mathrm{d}z \\ &= \int_{-\frac{L}{2}}^{\frac{L}{2}}\int_{-\pi}^{\pi}\left[\begin{array}{l} e^{-2j\xi p\alpha}\cdot\cos^2\left(m\frac{\pi}{L}z\right)\cdot\sin(\mu Q_s\alpha)\cdot\cos\left(\mu Q_s\frac{z}{L}\theta\right) \\ +e^{-2j\xi p\alpha}\cdot\cos^2\left(m\frac{\pi}{L}z\right)\cdot\cos(\mu Q_s\alpha)\cdot\sin\left(\mu Q_s\frac{z}{L}\theta\right)\end{array}\right] \\ &\quad\times\mathrm{d}\alpha\,\mathrm{d}z \\ &= \int_{-\frac{L}{2}}^{\frac{L}{2}}\left[\cos^2\left(m\frac{\pi}{L}z\right)\cdot\cos\left(\mu Q_s\frac{z}{L}\theta\right)\right]\mathrm{d}z \\ &\quad\cdot\int_{-\pi}^{\pi}\frac{e^{j\mu Q_s\alpha}-e^{-j\mu Q_s\alpha}}{2}e^{-2j\xi p\alpha}\,\mathrm{d}\alpha \\ &\quad+\int_{-\frac{L}{2}}^{\frac{L}{2}}\left[\cos^2\left(m\frac{\pi}{L}z\right)\cdot\sin\left(\mu Q_s\frac{z}{L}\theta\right)\right]\mathrm{d}z \\ &\quad\cdot\int_{-\pi}^{\pi}\frac{e^{j\mu Q_s\alpha}+e^{-j\mu Q_s\alpha}}{2}e^{-2j\xi p\alpha}\,\mathrm{d}\alpha. \end{aligned} \tag{C-1} $$

Acknowledgment

This work was supported by the National Natural Science Foundation of China under Project 51875410.

References

[1] A. M. El-Refaie *et al.*, "Advanced high-power-density interior permanent magnet motor for traction applications," *IEEE Trans. Ind. Appl.*, vol. 50, no. 5, pp. 3235–3248, Sep. 2014.

[2] Y. Miao, H. Ge, M. Preindl, J. Ye, B. Cheng, and A. Emadi, "MTPA fitting and torque estimation technique based on a new flux-linkage model for interior-permanent-magnet synchronous machines," *IEEE Trans. Ind. Appl.*, vol. 53, no. 6, pp. 5451–5460, Nov./Dec. 2017.

[3] S. Zuo, F. Lin, and X. Wu, "Noise analysis, calculation, and reduction of external rotor permanent-magnet synchronous motor," *IEEE Trans. Ind. Elect.*, vol. 62, no. 10, pp. 6204–6212, Oct. 2015.

[4] W. Deng and S. Zuo, "Electromagnetic vibration and noise of the permanent-magnet synchronous motors for electric vehicles: An overview," *IEEE Trans. Transport. Electrific.*, vol. 5, no. 1, pp. 59–70, Mar. 2019.

[5] Z. Q. Zhu and D. Howe, "Influence of design parameters on cogging torque in permanent magnet machines," *IEEE Trans. Energy Convers.*, vol. 15, no. 4, pp. 407–412, Dec. 2000.

[6] C. Xia, Z. Chen, T. Shi, and H. Wang, "Cogging torque modeling and analyzing for surface-mounted permanent magnet machines with auxiliary slots," *IEEE Trans. Magn.*, vol. 49, no. 9, pp. 5112–5123, Jul. 2013.

[7] H. Karmaker and A. M. Knight, "Investigation and simulation of fields in large salient-pole synchronous machines with skewed stator slots," *IEEE Trans. Energy Convers.*, vol. 20, no. 3, pp. 604–610, Sep. 2005.

[8] E. Schmidt, M. Sušć, and A. Eilenberger, "Finite element analysis of a permanent magnet synchronous machine with an external rotor for a position sensorless control," in *Proc. Australas. Universities Power Eng. Conf.*, 2009, pp. 1–6.

[9] S. Ruoho, E. Dlala, and A. Arkkio, "Comparison of demagnetization models for finite-element analysis of permanent-magnet synchronous machines," *IEEE Trans. Magn.*, vol. 43, no. 11, pp. 3964–3968, Nov. 2007.

[10] P. Wendling, Y. LeFloch, P. Lombard, A. Akabar, and L. Sabi-haddad, "Two techniques for modeling an induction motor with skewed slots with time-stepping 2D–3D finite element method," in *Proc. IEEE Int. Conf. Electr. Mach. Drives*, May 2005, pp. 1006–1010.

[11] X. Zhu, Z. Xiang, L. Quan, Y. Chen, and L. Mo, "Multimode optimization research on a multiport magnetic planetary gear permanent magnet machine for hybrid electric vehicles," *IEEE Trans. Ind. Electron.*, vol. 65, no. 11, pp. 9035–9046, Nov. 2018.

[12] L. Ding, G. Liu, Q. Chen, and G. Xu, "A novel mesh-based equivalent magnetic network for performance analysis and optimal design of permanent magnet machines," *IEEE Trans. Energy Convers.*, vol. 34, no. 3, pp. 1337–1346, Sep. 2019.

[13] Z. Q. Zhu, D. Howe, E. Bolte, and B. Ackermann, "Instantaneous magnetic field distribution in brushless permanent magnet DC motors. I. Open-circuit field," *IEEE Trans. Magn.*, vol. 29, no. 1, pp. 124–135, Jan. 1993.

[14] Q. Yu, X. Wang, and Y. Cheng, "Electromagnetic modeling and analysis of can effect of a canned induction electrical machine," *IEEE Trans. Energy Convers.*, vol. 31, no. 4, pp. 1471–1478, Dec. 2016.

[15] Q. Yu, X. Wang, and Y. Cheng, "Electromagnetic calculation and characteristic analysis of can effect of a canned permanent magnet motor," *IEEE Trans. Magn.*, vol. 52, no. 12, pp. 1–6, Dec. 2016.

[16] T. Lubin, S. Mezani, and A. Rezzoug, "Exact analytical method for magnetic field computation in the air gap of cylindrical electrical machines considering slotting effects," *IEEE Trans. Magn.*, vol. 46, no. 4, pp. 1092–1099, Apr. 2010.

[17] T. Lubin, S. Mezani, and A. Rezzoug, "2-D exact analytical model for surface-mounted permanent-magnet motors with semi-closed slots," *IEEE Trans. Magn.*, vol. 47, no. 2, pp. 479–492, Feb. 2011.

[18] L. Zhu, S. Z. Jiang, Z. Q. Zhu, and C. C. Chan, "Analytical methods for minimizing cogging torque in permanent-magnet machines," *IEEE Trans. Magn.*, vol. 45, no. 4, pp. 2023–2031, Apr. 2009.

[19] C. Xia, Z. Zhang, and Q. Geng, "Analytical modeling and analysis of surface mounted permanent magnet machines with skewed slots," *IEEE Trans. Magn.*, vol. 51, no. 5, pp. 1–8, May 2015.

[20] D. Žarko, D. Ban, and T. A. Lipo, "Analytical calculation of magnetic field distribution in the slotted air gap of a surface permanent-magnet motor using complex relative air-gap permeance," *IEEE Trans. Magn.*, vol. 42, no. 7, pp. 1828–1837, Jul. 2006.

[21] N. Elloumi, M. Bortolozzi, and A. Tessarolo, "On the analytical determination of the complex relative permeance function for slotted electrical machines," in *Proc. Int. Conf. Electr. Mach. (ICEM)*, Aug. 2020, pp. 253–258.

[22] Q. Yu and D. Gerling, "Analytical modeling of a canned switched reluctance machine with multilayer structure," *IEEE Trans. Magn.*, vol. 49, no. 9, pp. 5069–5082, Sep. 2013.